A Global Ocean-Atmosphere Climate Model. Part II. The Oceanic Circulation

KIRK BRYAN, SYUKURO MANABE AND RONALD C. PACANOWSKI

Geophysical Fluid Dynamics Laboratory/NOAA, Princeton University, Princeton, N. J. 08540

(Manuscript received 8 February 1974, in revised form 28 June 1974)

ABSTRACT

A numerical experiment has been carried out with a joint model of the ocean and atmosphere. The 12-level model of the world ocean predicts the fields of horizontal velocity, temperature and salinity. It includes the effects of bottom topography, and a simplified model of polar pack ice. The numerical experiment allows the joint ocean-atmosphere model to seek an equilibrium over the equivalent of 270 years in the ocean time scale. The initial state of the ocean is uniform stratification and complete rest. Although the final temperature distribution is more zonal than it should be, the major western boundary currents and the equatorial undercurrent are successfully predicted. The calculated salinity field has the correct observed range, and correctly indicates that the Atlantic is saltier than the Pacific. It also predicts that the surface waters of the North Pacific are less saline than the surface waters of the South Pacific in accordance with observations. The pack ice model predicts heavy ice in the Arctic Ocean, and only very light pack ice along the periphery of the Antarctic Continent.

The poleward heat transport of the model is very sensitive to the strength of the circulation in the vertical-meridional plane. The heat transport is strongest in the trade wind belt where Ekman drift and thermohaline forces act together to cause a net flow of surface water toward the poles. At higher latitudes in the westerly belt the wind and thermohaline forces on the meridional circulation tend to oppose each other. As a result, the heat transport is weaker. Heat balance computations made from observed data consistently show that the maximum heat transport by ocean currents is shifted 10°–20° equatorward relative to the maximum poleward heat transport by the atmosphere in middle latitudes. The effect of the zonal wind in enhancing poleward heat transport at low latitudes and suppressing it in middle latitudes is offered as an explanation.

1. Introduction

In Part I of this series (Manabe *et al.*, 1975) the state of the atmosphere is described for two numerical experiments with a global climatic model. In one experiment the ocean is purely passive, and serves only as an infinite source of water for surface evaporation. In a second experiment the effect of heat transport by ocean currents is included. The ocean model is allowed to take over part of the task of transporting excess heat received in the tropics to higher latitudes. A careful comparison of these two experiments allows a better understanding of how the ocean and atmosphere work together to produce a climate. This paper is devoted to a description of the ocean component of the model both from the standpoint of method and results obtained.

Although the atmosphere and ocean models used in this experiment have roughly the same horizontal resolution and the same number of levels, the atmospheric model requires two orders of magnitude more time steps to simulate a unit period of time than the ocean model. This large difference is due to the relatively low speed of currents and internal waves in the ocean, coupled with the fact that fast moving external waves can be filtered out of the ocean model with little loss of accuracy in the lower frequencies important in large-scale air-sea interaction. In units of mass per unit time the observed intensity of the ocean circulation is comparable to that of the atmosphere. The mass of the ocean, however, is 400–500 times greater. As a result, the "turnover" time of the ocean is very much longer than the atmosphere, giving a very long response time to changes in external boundary conditions. In a climatic calculation the long response time of the ocean model tends to offset the advantage of a longer time step.

In the previous study by Manabe and Bryan (1969) there was a factor of 100 between the time frame of the atmosphere and the ocean models. In the present study the same approach is used with the difference increased to 320. In practice, fluxes of momentum, heat and water calculated by the atmospheric model in a unit period are low-pass filtered with respect to time, and applied to the ocean model over the equivalent of 320 units of time. Seasonal variations of solar insolation must be omitted, an important simplification required by this non-synoptic method of coupling the ocean and atmosphere.

The world ocean circulation is a vast system. To cover the entire globe entails a significant loss of horizontal resolution compared to earlier studies of individual ocean basins [e.g., Cox's (1970) study of the Indian Ocean]. For climatic studies, however, it is vital to have global models synthesize and test the results of simpler models. The Northern and Southern Hemispheres have quite different ocean circulation patterns, illustrating the critical importance of geometry in the ocean circulation. The study of water mass properties show that very remote portions of the world ocean are intimately connected together by the abyssal thermal-haline circulation. Cold, dense water formed in the

Norwegian Sea can be traced into the Southern Hemisphere, and water formed at the surface near the coasts of Antarctica can be found in both the North Altantic and North Pacific. The formation and movement of the great water masses of the world ocean are important in the heat balance of the ocean, and therefore must be important in climate. These considerations motivated the present model in which the entire world ocean is included. While the mathematical model itself is quite general, the coarse resolution does not allow ocean currents to reach their full intensity. In this sense the present study must be considered preliminary, to be superseded later by similar, but more detailed calculations.

2. Equations of the model

The physical model of the ocean is similar to the one used in the earlier climatic study by the authors (Manabe and Bryan, 1969), but the numerical method is based on a new staggered grid formulation discussed by Bryan (1969) and Cox (1970). The different numerical formulation allows a realistic bottom topography to be included in the ocean model. Another new feature that has been added is a parameterization of forced convection in the mixed layer just below the ocean surface.

The essential simplifications of the model are the hydrostatic assumption, the Boussinesq approximation with respect to density variations, and a closure approximation for small-scale motions based on the turbulent viscosity hypothesis. Let $\mathbf{v}$ be the horizontal velocity vector, and ∇ the horizontal grad operator. The equation of motion and the hydrostatic relation may be written

$$\mathbf{v}_t+\mathbf{v}\cdot\nabla\mathbf{v}+w\mathbf{v}_z+(2\Omega+\dot{\lambda})\sin\phi\mathbf{k}\times\mathbf{v}=-\frac{1}{\rho_0}\nabla p+\kappa\mathbf{v}_{zz}+\mathbf{F}, \quad (1)$$

$$\rho g=-p_z, \quad (2)$$

where ϕ is the latitude, λ the longitude, $\dot{\lambda}$ the angular velocity relative to the rotating coordinate system and κ the coefficient of turbulent mixing in the vertical. Other symbols have their usual meanings, z and w being positive upward. $\mathbf{F}$ is a horizontal body force due to lateral mixing of momentum. In terms of a spherical coordinate system

$$F^{\lambda}=\frac{1}{a\cos\phi}\left[(\tau^{\lambda\lambda})_{\lambda}+\frac{1}{\cos\phi}(\cos^2\phi\tau^{\lambda\phi})_{\phi}\right], \quad (3)$$

$$F^{\phi}=\frac{1}{a\cos\phi}\left[(\tau^{\phi\lambda})_{\lambda}+\frac{1}{\cos\phi}(\cos\phi\tau^{\phi\phi})_{\phi}+\sin\phi\tau^{\lambda\lambda}\right], \quad (4)$$

TABLE 1. Values of the principle parameters in cgs units. The arrows indicate the adopted time span for given values of the parameters.

Parameter	Years 0	50	100	150	200	250
κ	1.0 ⟶		⟵		0.3 ⟶	
A_H	2×10^8 ⟶	⟵	5×10^7 ⟶	⟵	2.5×10^7 ⟶	
A_M	4×10^9 ⟶					8×10^9

where

$$\left.\begin{aligned}\tau^{\lambda\lambda}&=-\tau^{\phi\phi}=A_M D_T\\ \tau^{\lambda\phi}&=\tau^{\phi\lambda}=A_M D_S\end{aligned}\right\}, \quad (5)$$

D_S and D_T being defined in Part I, Section 2e. Note that the model is based on the ϕ, λ, z coordinate system. The formulation of friction given by (3), (4) and (5) is essentially a linearized version of that in the meteorological model.

The equation of continuity and equation of state are

$$w_z+\nabla\cdot\mathbf{v}=0, \quad (6)$$

$$\rho=\rho(\theta,S,p). \quad (7)$$

In the model the right-hand side of (7) is approximated by a polynomial, whose coefficients are fitted to the standard Knudsen formula. Details are given by Bryan and Cox (1972).

The conservation equations for potential temperature (θ) and salinity (S) under conditions of stable stratification are

$$(\theta,S)_t+\mathbf{v}\nabla(\theta,S)+w(\theta,S)_z=\kappa(\theta,S)_{zz}+A_H\nabla^2(\theta,S). \quad (8)$$

Note that unlike the atmospheric model A_H and A_M are constants, but in the course of the calculations several values of the parameters are used in different stages. Table 1 shows these regimes. The method of choosing the parameter A_M deserves more detailed explanation. The condition of no-slip at the lateral walls requires that a viscous boundary layer be resolved at the side walls. If this boundary is not resolved the error excites a computational mode that extends out into the interior, resulting in a checkerboard pattern in the streamfunction. The viscous boundary layer width according to Munk (1950) is

$$\Delta<L_M=\frac{\pi}{\sqrt{3}}(A/\beta)^{\frac{1}{3}}.$$

Therefore a given grid spacing Δ requires that

$$A>\beta(\Delta\sqrt{3}/\pi)^3.$$

Another criterion arises through the inaccuracy of the finite-difference model at the smallest scales that can be resolved.

Even in a completely stable computation a computational mode can be excited when centered differencing

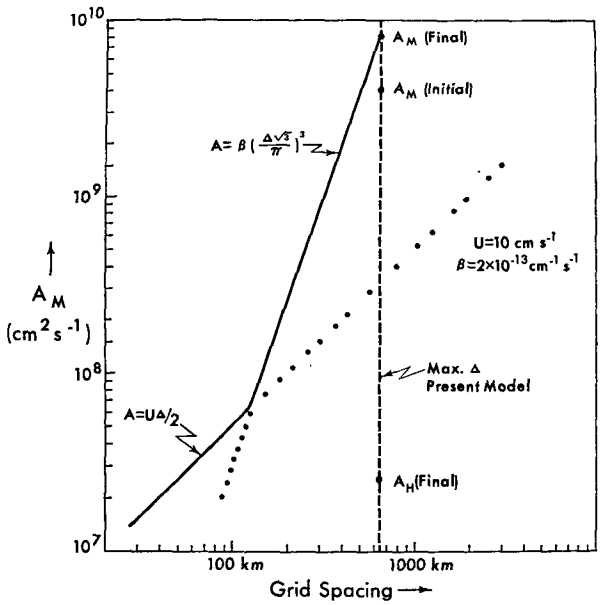

FIG. 1. Resolution criterion for determining the value of A_M in the finite-difference model. The steep curve is the requirement based on the Munk viscous boundary layer.

is used if the Reynolds number is not less than a certain critical value. The criterion derived by Chen (1971) is

$$\mathrm{Re}_{\mathrm{grid}}=U\Delta/A_M<2.$$

Chen's (1971) derivation is given in Appendix B. It turns out that the criterion above is a necessary, but not a sufficient criterion for the existence of the computational mode. Under certain circumstances smooth solutions are obtained for values of $\mathrm{Re}_{\mathrm{grid}}<2$. This is particularly true for cases with smooth inflow or initial value problems. However, once a computational mode is excited it is apt to remain in the solution unless the above criterion is satisfied. These two requirements are illustrated in Fig. 1. Values of A_M above the solid line will allow smooth solutions for a finite-difference model with second-order differencing. Values below the line may permit the growth of a computational mode.

The time stepping is carried out with alternate application of centered and forward time steps in a ratio of 17:1. The centered time steps are second-order accurate, but contain a weak instability. This instability is suppressed by infrequently taking a forward time step.

Due to the strong geostrophic coupling between the velocity and the density field at most latitudes, a computational mode in the density field tends to be suppressed through the viscosity working on the velocity field. Thus the lateral diffusion of temperature and salinity can be much less than the value required for A_M. Note that in the course of the experiment A_H is decreased in two steps from 2×10^8 to 2.5×10^7 cm s^{-1}. A further decrease of A_H seemed likely to excite the computational mode and produce an inaccurate numerical solution.

Computational considerations are not so important in the choice of κ, the vertical mixing coefficient. The vertical resolution of the model is good enough to allow a choice of κ well within the range estimated from observations. Stommel and Webster (1962) estimated that κ lies within a range from 1.0–0.1 cm^2 s^{-1} based on the density structure of the thermocline. Using geochemical data for the lower thermocline in the Pacific, Munk (1966) obtained an estimate of 1.3 cm^2 s^{-1}. Recently a study of tritium data in the North Atlantic by Rooth and Östland (1972) and direct measurements of thermal turbulence in the thermocline by Osborne and Cox (1972) suggest values in the low end of the range given by Stommel and Webster (1962). Accordingly, the value of 1.5 cm^2 s^{-1} used in the air-sea model of Manabe and Bryan (1969) has been reduced. Note that the final value in Table 1 is 0.3 cm^2 s^{-1}.

Since convective mixing has a very small horizontal scale it cannot be handled explicitly in a large-scale numerical model. We therefore impose a constraint which models free convection. The constraint cannot be easily expressed in analytic form, but is applied as follows: if (8) predicts an unstable stratification at any given time step, the predicted values of potential temperature and salinity are adjusted so that all quantities are conserved and the vertical gradients vanish. Following the adjustment for free convection an additional correction is made for mixing due to wind. The model is suggested by the energetic approach of Kraus and Turner (1967). Let u^* be the friction velocity equal to $|\tau^s/\rho_a|^{\frac{1}{2}}$, where τ^s is the surface stress and ρ_a the air density. Over two time steps the energy fed into the ocean by the wind may be estimated as

$$\Delta K=2\Delta t\rho_a(u^*)^3. \tag{9}$$

The potential energy of the water column is

$$P=\int_{-H}^{0} z\rho g dz. \tag{10}$$

In our simple parameterization the depth of the mixed layer is extended downward conserving heat and salinity. The increase in depth of the mixed layer is governed by the constraint that

$$\Delta P=\Delta K\times\text{constant}. \tag{11}$$

A description of the model is incomplete without a specification of boundary conditions. At the lateral walls

$$v=(\theta,S)_n=0, \tag{12}$$

where $(\ )_n$ denotes the local derivative with respect to the coordinate normal to the wall.

At the ocean bottom

$$\left.\begin{aligned} w&=-\mathbf{v}\nabla H\\ \mathbf{v}_z&=(\theta,S)_z=0\end{aligned}\right\} Z=-H. \tag{13}$$

TABLE 2. Depth of various levels in the numerical model and the horizontally uniform initial values for potential temperature and salinity.

k	Depth	Initial θ	Initial S
1	25	17.46	34.74
2	85	15.42	34.96
3	169	12.61	34.99
4	295	9.88	34.85
5	482	7.46	34.69
6	754	5.33	34.59
7	1130	3.75	34.62
8	1622	2.76	34.70
9	2228	2.15	34.74
10	2935	1.75	34.74
11	3721	1.48	34.73
12	4565	1.34	34.73

At the surface

$$w=0, \tag{14}$$

$$\kappa(\mathbf{v})_z=\boldsymbol{\tau}^s(\phi,\lambda). \tag{15}$$

The surface boundary conditions on temperature and salinity will be specified later in connection with the ice model.

3. Numerical grid and time-dependent behavior of the ocean model

The horizontal spacing of points in the ocean numerical model corresponds exactly to that of the atmospheric model. Unlike the atmospheric model, however, all predicted variables are not defined at the same points. Following a method given in Bryan (1969) the horizontal layout is like a checkerboard. Temperature, salinity and the transport streamfunction are defined at the center of each square and velocity at the corner points. There are 12 levels in the vertical. These levels (shown in Table 2) are selected to give the maximum resolution in the upper thermocline, where heat exchange with the atmosphere is most important.

The finite-difference grid system is based on ordinary spherical coordinates. This approach is very straightforward, but grid points become very closely crowded together along latitude circles in the vicinity of the poles. The time step used for predicting variables must satisfy the Courant-Friedrichs-Lewy condition over the entire region. For zonal flow (U)

$$\Delta t < U/(2\Delta\lambda \cos\phi),$$

and the maximum step allowed would depend on the points closest to the poles. As in the atmospheric model, Fourier filtering is used to deal with this problem. Poleward of 45N and 45S a low-pass filter is applied at each time step so that the predicted variables have the same east-west scale at all latitudes. Due to the existence of land boundaries enclosing the ocean basins, the formulation must be somewhat different than that of the atmospheric model. Using the rigid-lid approximation to filter out external gravity waves, the most stringent condition on the time step is due to large-scale external Rossby waves. Since this study is concerned with a final equilibrium solution rather than the transient behavior, the external and internal modes are numerically integrated with different time steps. The result is a very great increase in efficiency of the ocean calculation relative to the Manabe and Bryan (1969) study. Details are given in Appendix A.

Velocity components are zero at the walls. They must therefore be expanded in a sine series along latitude circles. Let i be the index of grid points in the direction of increasing longitude. Then

$$(u,v)_i=\sum_{m=1}^{M'}[U_m(\phi),V_m(\phi)]\sin\left(\frac{m\pi i}{M+1}\right), \tag{16}$$

where

$$M'=\text{Integer}\,[M\cos\phi+0.5], \tag{17}$$

and M is the total number of grid points between two land boundaries at any given level in the ocean. Boundary conditions on velocity are automatically satisfied at $i=0$ and $M+1$. Temperature and salinity obey zero flux conditions at the walls of ocean basins, and therefore are expanded in a cosine series:

$$(\theta,S)_i=\sum_{m=0}^{M'-1}[\theta_m(\phi),S_m(\phi)]\cos\left[\frac{(i+\frac{1}{2})\pi m}{M+1}\right]. \tag{18}$$

In this case boundary conditions are automatically satisfied at $i=\frac{1}{2}$ and $i=M+\frac{1}{2}$.

The bottom configuration of the ocean for the joint air-sea model is shown in Fig. 2. It is based on much more detailed topography given by Smith *et al.* (1966), but modified by expanding in spherical harmonics, and truncating the series to be compatible with the resolution of the model.

As noted earlier, the initial temperature and salinity distribution is a function only of z and the fluid is in a state of complete rest. The main features of the thermocline develop during the first 40–50 years in the ocean time frame. Subsequent changes are of two types. One type is concentrated near the surface. In this region the response of the ocean is rapid. However, the coupling between the atmosphere and the ocean is such that a six-month change in the atmospheric model shows up as a 50-year change in the ocean time frame. Thus the slow rate of change shown in Fig. 3 is associated with the boundary fluxes themselves rather than the response of the upper ocean.

A second type of change takes place in the deep ocean. In the deep ocean the expected response time of the ocean is orders of magnitude greater than that near the surface (Bryan and Cox, 1968). The initial temperature and salinity correspond to the properties of deep water actually observed. On the other hand, the climate of the joint model does not correspond closely enough with the observed climate to produce deep water that is as cold as observed. As a result there is a

FIG. 2. The smoothed topography of the ocean model. Depth is given in kilometers.

dense mass of isolated deep water in the model ocean that is slowly heated as the experiment proceeds. The trend is evident in Fig. 3. Temperature has been plotted on a logarithmic scale in Fig. 3 so that small, but significant changes in the deep water show up more clearly.

Note that there is a very strong warming trend in the upper ocean during the first 50 years. This reflects a general deepening of the thermocline which persists through the second century of the simulation even though the vertical mixing has been decreased from 1.0 to 0.3 $cm^2\ s^{-1}$. The differences in temperature between the year 100 and 200 amount to the equivalent of a net change in heat of the entire water column of 58.3 kcal cm^{-2}. If this is converted to a heating rate at the surface, it amounts to 1.1×10^{-5} ly min^{-1}. While this is a net heat sink for the atmosphere averaged over this period, it is not a very significant one. The normal heating and cooling rates at the ocean surface are at least three orders of magnitude greater (Budyko *et al.*, 1962).

4. Sea ice

The sea ice model can be expressed in a single equation. Let I be the local ice thickness (assumed to be uniform), and Q_a and Q_b the heat flux received at the base of the floating ice from above and below, respectively. We let S_n^* and E^* be the contributions to ice gain and loss due to snowfall and evaporation. Then

$$I_t=-\nabla(\delta_I \mathbf{v} I)+A_H\nabla^2 I+S_n^*-E^* -(Q_a+Q_b)/(\rho_I L_f), \quad (19)$$

where ρ_I and L_f are the density of ice and the latent heat of freezing. We take

$$\delta_I=\begin{cases}1, & I<4\text{ m}\\ 0, & I>4\text{ m}\end{cases} \quad (20)$$

where δ_I is a kronecker delta which parameterizes the ice jamming which occurs when ice builds up beyond a given thickness; $\mathbf{v}$ is simply the velocity of the water in the top layer of the ocean model. Certain shortcomings of this oversimplified treatment of ice dynamics will be apparent in the results of the joint ocean-atmosphere calculation.

In ice-free areas the heat flux is calculated from the equations of surface heat balance with the surface temperature taken to be equal to temperature at level 1. In areas covered by ice the surface temperature T^* is calculated from the equations of surface heat balance, where Q_a is the flux of heat downward into the ice:

$$Q_a=k(T^*-271.2)/(I+1.7). \quad (21)$$

If the calculated value of T^* is greater than 273 K, it is set equal to 273, and Q_a is calculated from the surface heat balance. This corresponds to melting conditions in the ice pack. The heat flux from below is taken as

$$Q_b=\kappa(\theta_1-271.2)/|z_1|. \quad (22)$$

The thermal conductivity k is an average value determined from observation (5×10^{-3} cal $cm^{-2}\ s^{-1}$); and θ_1 and z_1 are the temperature and the depth of the first level.

The surface flux of water is determined by the values of evaporation minus precipitation in ice-free areas. In ice-covered areas the effects of melting and freezing

of ice are carefully taken into account so that water is covered for the whole system.

In the initial state there is no pack ice in any part of the model ocean. The steady buildup of pack ice which occurs as time goes on is shown in Table 3. Growth of sea ice starts in the Arctic Ocean and soon spreads into the North Atlantic and Bering Straits. The maximum thickness occurs in the vicinity of the North Pole. Actual observations indicate an export of ice from the Arctic into the Greenland Sea. Untersteiner (1964) estimates this export to be 30 megatons per year, equivalent to a loss of 20 cm of ice per year over the whole Arctic Basin. If a mechanism of this sort were present in the model, it would have prevented the ice buildup shown in Table 3. Instead, the ice in the model rapidly builds up beyond the critical thickness ($I>4$ m) over most of the Arctic and from that point in time onward all motion stops, making ice export from the Arctic Basin impossible.

A small amount of ice forms in the Southern Hemisphere. In only a few localized portions of the Ross Sea and the Weddell Sea the ice reaches a thickness >1 m. Most of the sea ice in the Southern Hemisphere forms annually and perennial sea ice exists only in a few locations. Thus the great difference between the Arctic and the Antarctic ice in the model is not incompatible with observations.

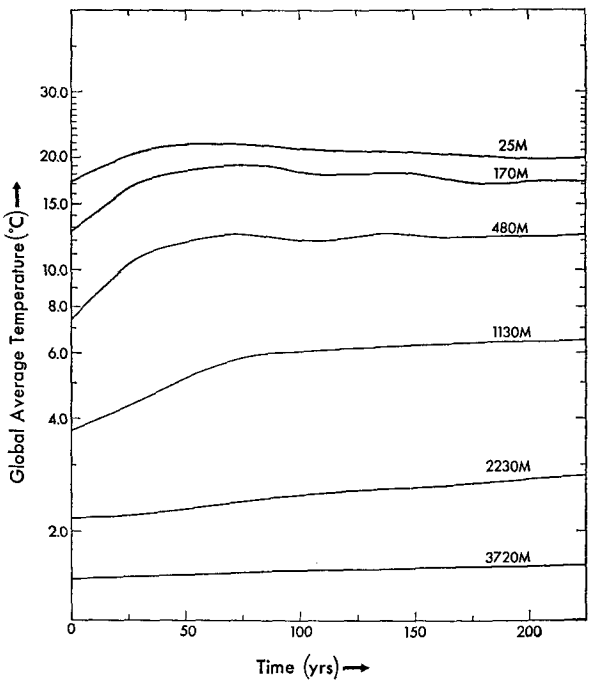

FIG. 3. Horizontally averaged temperature over the entire domain as a function of time. Note the initial deepening of the thermocline.

5. Horizontal velocity and salinity fields

From this point on the final fields obtained by averaging from year 220–270 will be discussed. To introduce a description of the velocity field of the ocean model it is necessary first to examine the zonally averaged surface stress. In Fig. 4 this stress is compared with an estimate based on actual data by Hellerman (1967). We can only understand various features of the ocean model fields if we note the differences between the boundary condition on the real ocean and the boundary condition on the model. Note that the agreement between zonally averaged wind stresses observed and computed is quite close in the Northern Hemisphere. The principle lack of agreement is in the Southern Hemisphere poleward of 30S. As mentioned in Part I the "roaring forties" seem to be missing entirely from the model and there is even a narrow belt of surface easterlies at 50S.

The Ekman transport in the planetary boundary of the ocean is in a direction 90° to the right of the surface stress in the Northern Hemisphere. It is equal to the surface stress divided by the Coriolis parameter. Upwelling due to wind is the horizontal divergence of the Ekman transport, i.e.,

$$W_{up}=\nabla\times(\tau^s/2\Omega\sin\phi). \tag{23}$$

A comparison of upwelling computed in the air-sea model and upwelling calculated from observed wind stresses is allowed by Fig. 5. In the Northern Hemisphere agreement is not unsatisfactory. In both cases there are broad regions of downwelling in the subtropics and upwelling at higher latitudes. Although more restricted in area in the model, there are upwelling regions along the eastern margins of the Atlantic and Pacific corresponding to observations. These upwelling regions off Africa and Mexico are very important in the local climate.

Equatorial upwelling exists at all longitudes using both the observed and calculated wind-stress patterns. The difference lies in the fact that the zone of upwelling in the air-sea model is wider and consequently weaker. In the Southern Hemisphere agreement in the upwelling patterns shown in Figs. 5a and 5b is poor. This might be anticipated from the differences in the zonally average wind stress shown in the previous figure. Between 10–30S the gradient in the north-south direction of the winds stress is the same. In this belt downwelling occurs in both the observed and calculated patterns. Poleward of 30S agreement breaks down completely. The narrow belt of easterlies near 50S leads to a zone

TABLE 3. A summary of the total area and average thickness of sea ice at different stages of the calculation.

Pack ice parameter	Year 0	50	100	150	200
Area of ice ($\times 10^6$ km^2)	0	17.8	26.9	39.5	37.4
Average thickness (m)	0	0.14	2.96	3.81	5.32
Maximum thickness (m)	0	1.6	12.7	19.1	24.7
Sea ice in Southern Hemisphere	no	no	no	yes	yes

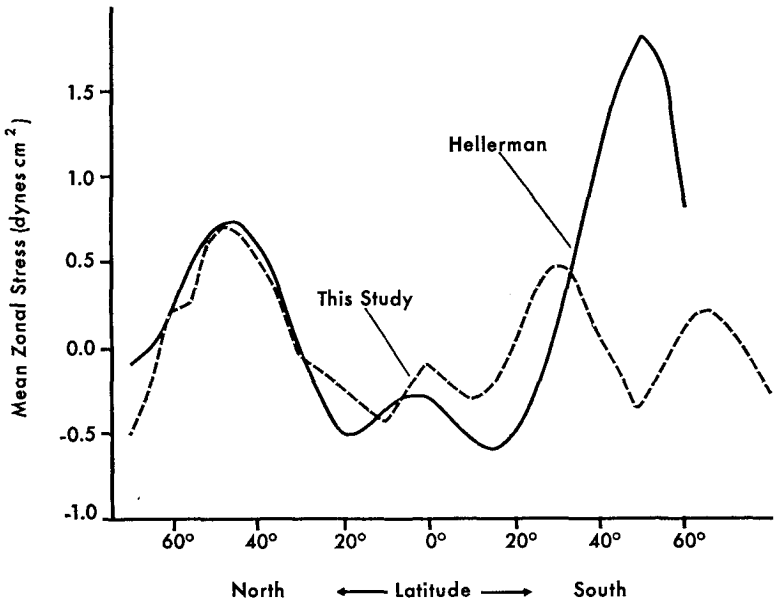

FIG. 4. A comparison of zonally averaged stress calculated in the model with a stress estimate based on observations by Hellerman (1967).

of downwelling in the model, where upwelling would normally occur. There is probably a strong connection between the downwelling belt and the anomalously warm surface temperatures of the ocean model in this latitude zone noted earlier in Part I.

In spite of the rather large differences between the observed mean annual wind stress and the computed pattern, the overall current structure in the upper ocean is surprisingly realistic. The pattern of currents at the top level shown in Fig. 6b may be compared to observed surface currents in Fig. 6a. Along the equator there is a strong tendency for the computed currents to diverge much more strongly than the observed surface drift. This can be accounted for by the fact that the computed currents represent an average over the entire Ekman layer. Currents averaged over a deeper layer must have stronger rotation away from the surface stress vector than surface drift currents. At the equator itself the surface currents are westward at the surface, but become eastward at the 169 m level shown in Fig. 6b. Note how much more coherent the currents at the 169 m level are than at the surface where the wind drift obscures detail.

Vigorous cyclonic gyres in subtropical latitudes are present close to their observed positions. One obvious discrepancy is that the Pacific subtropical gyre extends too far to the north, so that the subarctic gyre is pushed into a very narrow band of latitudes near the northern boundary. The subarctic gyre in the North Atlantic is better developed, but the extension of the Gulf Stream tends to go directly eastward rather than penetrate into the Norwegian Sea as observations indicate.

Another missing feature is the Agulhas Current off the southeast tip of Africa. Observations show the Agulhas as a western boundary current which flows along the eastern coast of Africa to its southern tip. In the model, however, the western boundary current off of Africa separates from land near Madagascar. The main source of the discrepancy is the simplified geometry of the model. If the western boundary current were allowed to flow in the Mozambique Channel between Madagascar and the mainland this separation would probably occur further south.

In order to compare with estimates for the real ocean the transport of major currents is given in Table 4. Note that the model underpredicts the maximum transport of most of the major currents by large factors. In the case of the Antarctic current the wind stress provided by the atmospheric model is obviously too weak. In the case of the Northern Hemisphere western boundary the discrepancy is probably due to the model itself. So far no analytic nor numerical model has been able to account for transports as large as those observed

TABLE 4. Transport (megatons per second) for the model compared to estimates for the real ocean.*

Current system	Model transport	Estimated *maximum* transport
Gulf Stream	14	100– (1)
Labrador	12	–
Brazil	14	–
East Australian	24	20–43 (2)
Kuroshio	20	80–90 (3)
Agulhas	20	–
Circumpolar	22	0–230 (4)

* References are: (1) Warren and Volkmann (1968); (2) Hamon (1965); (3) Worthington and Kawai (1972); (4) Reid and Nowlin (1971).

FIG. 5a. Upwelling in the surface layer based on a different model with 1°×1° mesh and Hellerman's (1967) wind stress data.

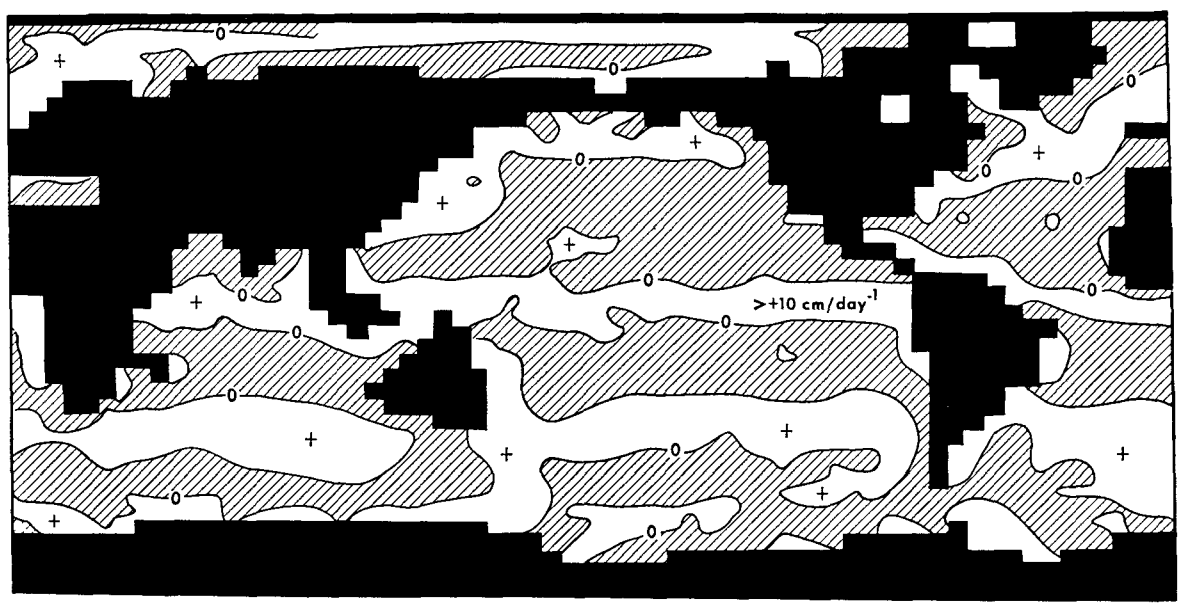

FIG. 5b. Upwelling pattern based on the present model (only the sign is shown).

by Warren and Volkmann (1968) in the Gulf Stream. The failure of linear models driven by wind alone was first noted by Munk (1950). Bryan (1963) and Veronis (1966) used numerical models to show the enhancement of transport of western boundary currents by the addition of nonlinear terms to the homogeneous wind-driven ocean models of Munk (1950) and Stommel (1948), respectively. Sarkisyan (1966) in a series of papers has indicated the importance of bottom torques associated with baroclinicity and topography in modifying the pattern of total transport. Holland and Hirschman (1972) and Keondjian (1972) have made diagnostic calculations with the observed density field which predict transports less than, but much closer to, the observed values than any previous models. In the analysis of observed fluctuations in the Florida Current and the Gulf Stream, Webster (1961) showed that transient disturbances tend to cause a convergence of momentum into the Gulf Stream in the same way in which cyclones in the atmosphere enhance the jet stream. Although this effect is difficult to incorporate in a large-scale model, it will probably be necessary to include it for models of western boundary currents to be in satisfactory agreement with observations.

Although some features of the surface temperature pattern have been already discussed in Part I, this field is so important to a joint air-sea model that it is appropriate to discuss it in more detail in an oceanographic context. In the observed pattern shown in Fig. 7a we note that the temperature pattern is quite zonal in the Southern Hemisphere, but pronounced deviations from zonal symmetry are present in the North Atlantic and Pacific. These deviations reflect the anticyclonic circulation of the subtropical gyres, and

FIG. 6a. Observed surface drift currents based on Sverdrup *et al.* (1942) for February and March.

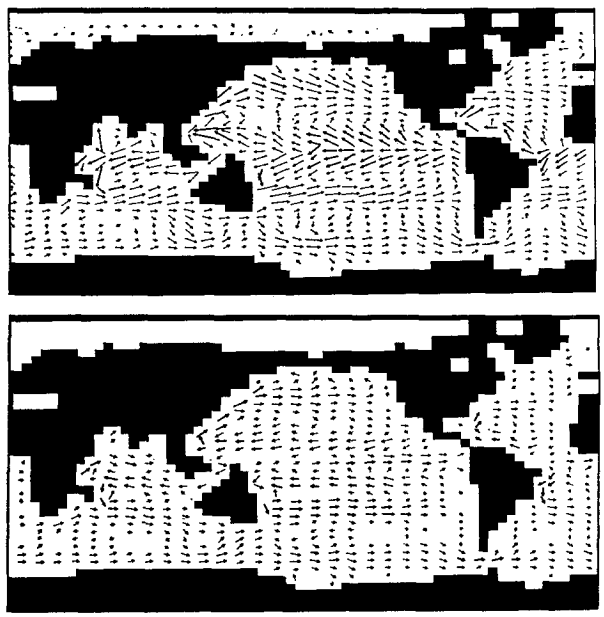

FIG. 6b. Velocity vectors at 25 m (top) and 169 m (bottom) in the model. Maximum currents in the Kuroshio are 30 cm s^{-1}. Heavy arrows represent currents of twice the velocity relative to thin arrows of the same length.

the cyclonic circulation of the subarctic gyres shown in Fig. 6a. The effect of these two gyres is to produce a weak gradient on the eastern side of the ocean basins and a tight gradient of the western side, which is associated with the extensions of the Gulf Stream and Kuroshio current.

Partly due to the lack of resolution and partly due to the weaker wind systems, the model ocean currents have much less intensity than those observed. As a result the heat transport by ocean currents does not have as strong an effect on the surface heat balance in critical regions as it should. The same is true at the equator. The observed pattern shows a pronounced temperature minimum in the eastern Pacific. In the computed pattern (Fig. 7b) the correct tendency is present, but the minimum is only about one-half that observed. This difference is quite critical since this area of the equatorial Pacific is believed to be very important in large-scale air-sea interaction. Another important difference between observed and computed temperature is in the Southern Hemisphere in middle latitudes. There is a broad zone in which the model temperature is much higher than that observed. As shown in Fig. 3 there is also a very strong difference in the zonal average of observed and computed winds in the Southern Hemisphere at these latitudes. This anomalous zonal wind distribution is present in the atmospheric model in both the case of an active and a passive ocean. Since the anomalous easterlies produce an Ekman transport toward the pole instead of toward the equator over a band of latitude from 40–60S, the computed surface temperatures are much higher than the observed temperatures in this zone.

We next turn to the field of salinity. Observed and calculated values can be compared in Fig. 8. Keeping in mind that the initial condition for the numerical experiment is one of horizontally uniform salinity at each horizontal level, the model is successful in predicting the observed range of salinity in surface waters. The model is also successful in predicting that the Atlantic in low latitudes is saltier than the Pacific by almost 1‰. In Table 5 the zonal average of precipitation and runoff minus evaporation is shown for the major oceans. The net water flux at the ocean surface shown in Table 5 represents an average over the final 50 years of the calculations. The net evaporation is clearly higher in the Atlantic than the Pacific, presumably due to the fact that the Atlantic is a narrow ocean downwind of the Sahara region, while the Pacific has a much more maritime climate. The surface salinities shown in Fig. 8b appear to be generally consistent with the values in Table 5, indicating that local surface sources and sinks of water are the leading factor controlling the surface salinity in the model.

The salinity in both the Indian Ocean and the Antarctic is overpredicted by about 1‰. The latter may be due to a lack of the seasonal formation of ice, and a northward export of ice which normally occurs around the Antarctic Continent. The most serious discrepancy is in the Norwegian Sea area in the North Atlantic. The model predicts a cold, fresh halocline over the entire area, such as observed only in the Arctic and Antarctic Oceans. Under present conditions warm salty water associated with an extension of the Gulf Stream flows into the Norwegian Sea where it is rapidly chilled to near freezing temperature. In our solution

TABLE 5. The zonal average of precipitation and runoff minus evaporation during the final period of the calculation. Units are centimeters per year.

Latitude	Oceans		
	Pacific	Atlantic	Indian
28.4N	−20	−34	
19.0N	−59	−83	
9.5N	−67	−82	−141
0.0	50	35	76
9.5S	31	−127	−39
19.0S	−80	−82	−103
28.4S	−25	−13	−35

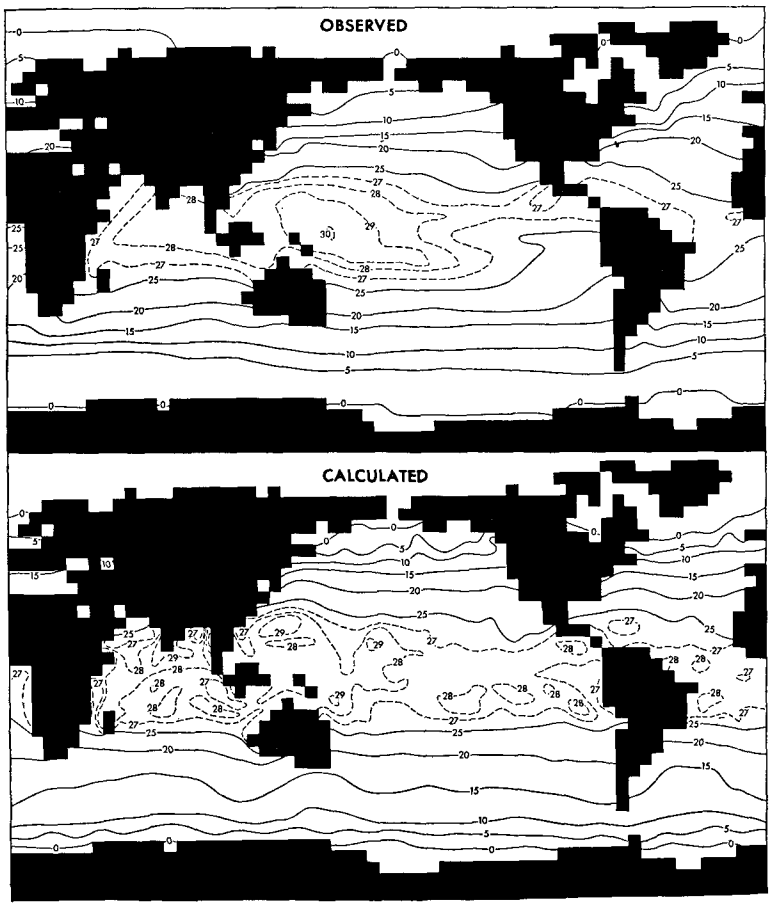

FIG. 7. Observed (a) and model computed (b) annual averaged surface temperatures.

the Gulf Stream extension moves along a nearly east-west line across the North Atlantic, so that the very cold water in the Iceland area is effectively isolated.

6. Vertical structure of the temperature and salinity fields

A picture of the three-dimensional structure of the temperature and salinity fields is provided by vertical, north-south cross sections for the Atlantic and Pacific shown in Figs. 9 and 10. The observed and predicted fields of temperature are shown in Fig. 9. Note that the upper kilometer of the ocean is shown in expanded scale to emphasize details of the thermocline. An obvious discrepancy between the calculated and observed fields is the overall thickness of the thermocline. The observed field shows that the 5°C isotherm is only below 1 km in the North Atlantic, where the lens of surface water associated with the subtropical gyre is anomalously deep. In the calculated sections, however, the 5°C isotherm is consistently below 1 km in both the Atlantic and Pacific. Although the calculated patterns show a weak tendency for the isotherms to be bowed upward near the equator, the isotherms are relatively flat compared to those observed. The relative importance of lateral mixing or lack of vigor in the thermohaline circulation in causing these differences will be discussed later.

In the calculated patterns the 5°C isotherm in deeper water outcrops at the surface only in the Southern Hemisphere in the vicinity of Antarctica. Surprisingly the 5°C water shown at the surface in the calculated pattern for the North Atlantic is an isolated patch of cold water associated with a halocline in the Norwegian Sea area. This feature is shown clearly in the salinity cross sections of Fig. 10. The salinity structure of the North Atlantic departs radically from that observed. In the observed section the North Atlantic is shown to be unusually saline with the 36.0‰ isoline penetrating below 0.5 km at 40N. No sign of the surface halocline shown in the observed data for the North Pacific is present in the North Atlantic. The 35.0‰ isoline outcrops at the surface in the observed North Atlantic section and the area near Iceland is considered a major area of deep-water formation. In the model solution the formation of deep water is completely cut off by the halocline at the surface. This feature is extremely interesting, because the formation of a halocline in the North Atlantic has been suggested as a mechanism for

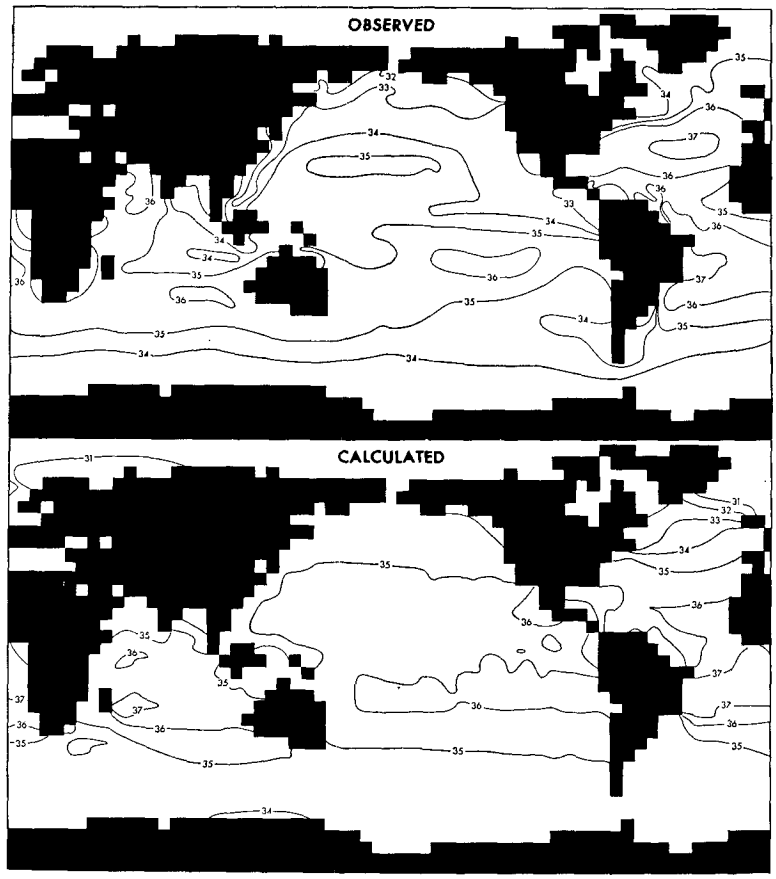

FIG. 8. Observed (a) and model-computed (b) surface salinities. Observed values are from Sverdrup *et al.* (1942).

causing ice ages by Weyl (1968). The effects of this feature of the model on the transport of heat by the Atlantic will be discussed later.

In connection with a discussion of surface salinity patterns it was noted earlier that the model predicts the South Pacific to be more saline than the North Pacific as observed. This is shown here clearly in the vertical cross sections. In both the observed and predicted patterns there is a large lens of water of salinity $>36.0‰$ in the South Pacific, but almost no water of this salinity in the North Pacific. A well-known feature of both the Atlantic and Pacific is the intrusion of Antarctic intermediate water of salinity $<34.5‰$ pushing northward at intermediate levels. Unfortunately, the model is unable to simulate this feature in either ocean.

7. Thermohaline circulation and poleward heat transport

The term thermohaline circulation refers to the large-scale, density-driven component of the ocean circulation. Due to important nonlinear terms in the governing equations it is by no means independent of the wind-driven component. However, the concept is still useful to organize the large amount of information needed to describe the ocean circulation. Since the initial horizontally uniform distribution of temperature and salinity were chosen from the area-averaged observed values for the world ocean, the initial deep water corresponds to the dense water being formed at polar latitudes under present climatic conditions. Since the computed climate will be different from the existing climate, there is a chance that the deep water formed by the model will be quite different from the initial water at the beginning of the numerical experiment. This is what actually occurs in the previous climatic experiment of Manabe and Bryan (1969), and the same effect exists in the present calculation. Due to the warmer than observed surface temperature around Antarctica, no deep water forms with a temperature much less than 4°C. As a result there is a layer of stagnant water at deeper levels which is bypassed by the thermohaline circulation. The replacement time for the deep water of the world ocean is equal to the total volume below the thermocline divided by the rate of

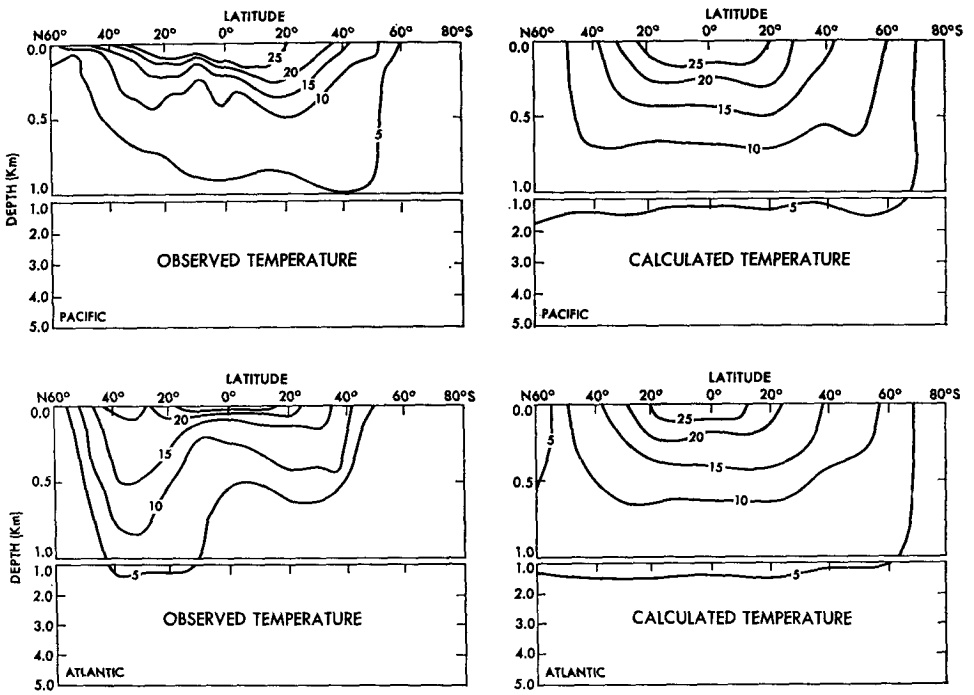

FIG. 9. Vertical north-south sections of temperature at 150W in the Pacific and at 30W in the Atlantic. Observed patterns are based on Reid (1965) and Sverdrup *et al.* (1942) for the Pacific and Atlantic, respectively. *N.B.* north is to the left.

deep water formation, i.e.,

$$\text{Replacement time} = \frac{\text{Volume of abyssal water}}{\text{Rate of abyssal water formation}}.$$

From Sverdrup *et al.* (1942) we estimate that the volume of the ocean below 2 km is approximately 5×10^8 km^3. The rate of bottom water formation is variously estimated between 20–60 megatons per second or $6\text{–}18\times10^5$ km^3 per year (Munk, 1966). The corresponding replacement time scale is 300–1000 years which makes it difficult to obtain a true climatic equilibrium for the deep water of the world ocean in a numerical experiment.

Transport streamlines for the vertical-meridional plane are shown in Fig. 11. All oceans are combined, and the units are megatons per second. The vertical scale has been expanded to show the upper 1000 m of the ocean in more detail. The first point to be noted about the pattern is that maximum values are only about 15 units except for an anomalous swirl right on the equator at mid-depths. Thus the model ocean is turning over at a much slower rate than the estimates for the real ocean given above indicate. It is also significant that the overturning is almost entirely confined to the upper kilometer, and the abyssal region of the model ocean is relatively quiet. The lack of abyssal overturning is associated with the initial conditions which are based on observed temperatures for the real ocean. Since the observed temperatures of the real ocean are much colder than the cold dense water formed by the model in polar regions, an isolated slowly warming water mass is created at depth. This water mass is simply bypassed by the meridional circulation.

A pair of features that stand out very clearly are two shallow cells on either side of the equator. These cells have been dominant in previous numerical studies (Bryan and Cox, 1968). The upper branch is due to Ekman drift away from the equator, and the lower branch is a geostrophic flow associated with the east-west pressure gradient in the trade wind zone. The upwelling at the equator due to Ekman drift divergence has already been shown in Fig. 5b. The anomalous circulation at deeper levels at the equator is entirely confined to the Indian Ocean. An analysis of this feature does not provide any clear explanation, except to suggest that the vertical resolution of the numerical model is not always adequate to handle the ageostrophic flow at the equator. In the Northern Hemisphere the flow of surface water is poleward from the equator to 50N. North of 30N the Ekman drift opposes the northward movement of surface water. As a result the poleward flow of water in the western boundary currents is almost entirely offset by the wind drift in the opposite direction in the surface layers. Thus the poleward movement of water only shows up strongly at lower levels. This feature is very important in the poleward transport of heat. The transport pattern in the Southern Hemisphere will not be discussed in detail, because it is

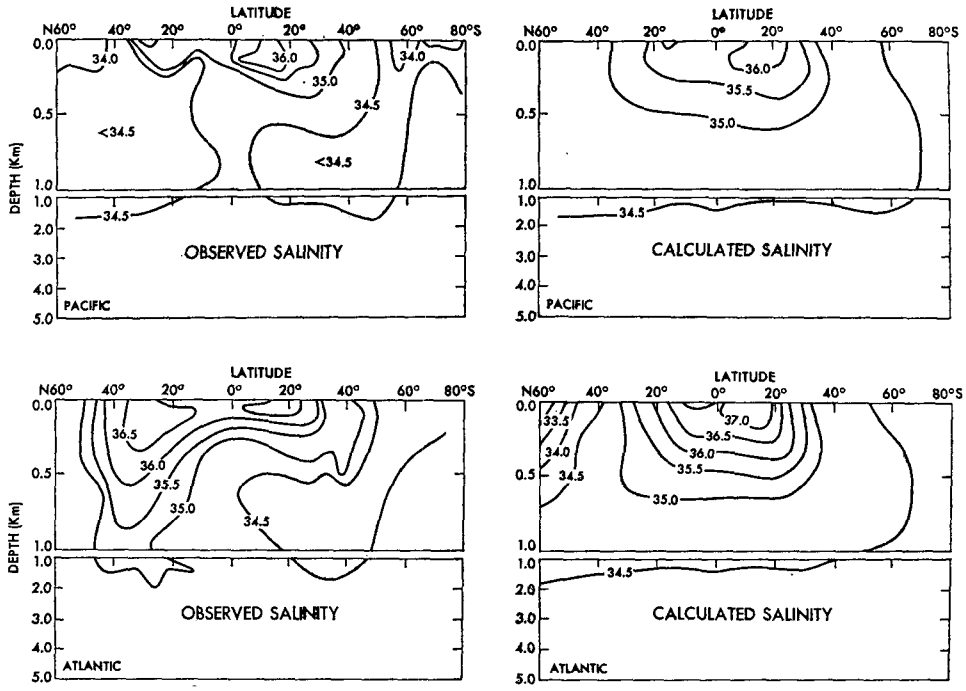

FIG. 10. Sections corresponding to Fig. 9 for salinity.

strongly influenced by the rather unrealistic zonal wind stress distribution shown in Fig. 4.

The basic role of air currents and ocean currents in climate is to transport heat from the tropics to higher latitudes. The heat transport is partitioned between the atmosphere and ocean in such a way that the atmosphere carries most of the heat poleward in middle latitudes with the ocean being more important at lower latitudes (see Fig. 19, Part I). The possibility that the partitioning of poleward heat transport changes with time may be an important factor in climate variations. For example, if the ocean could transport heat poleward more effectively than it does at present the poleward temperature gradients in the atmosphere would be less than they are at present, and *vice versa*. To gain a deeper understanding of this problem it is necessary to examine the various mechanisms by which the ocean can transport heat. Let $H(\phi)$ be the total heat transported poleward by ocean currents of the model ocean. Then

$$H(\phi)=\int_0^{2\pi}\int_{-H}^{0}\rho_0 C_p(a\theta V-A_H\theta_\phi)\cos\phi\, dz d\lambda.$$

The heat transport is due to the covariance of northward velocity and temperature, and horizontal diffusion.

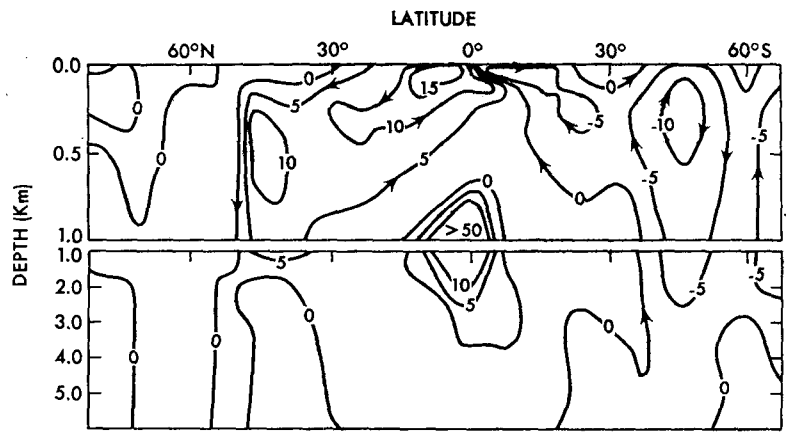

FIG. 11. Total transport of the world ocean model in the north-south vertical plane. Units are megatons per second.

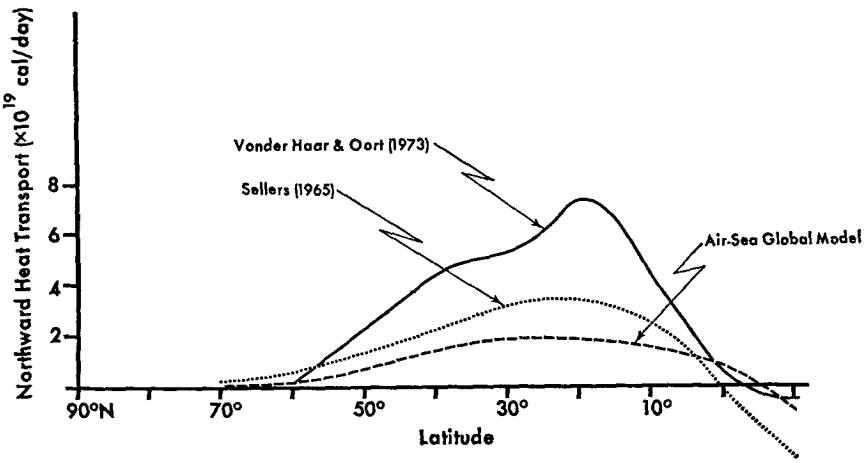

FIG. 12. Heat transport by the ocean model in a northward direction compared to estimates based on heat balance calculations.

Further, it is worthwhile to split the θV term in two components. One component is due to a correlation between the zonally averaged flow at each level and the zonally averaged temperature, and a remainder term associated with horizontal correlations along a latitude circle. The former we shall designate the *meridional cell component* and the latter a *gyre component.* Physically the first component may be thought of as the heat transport that takes place when warm surface waters move poleward, compensated by a return flow of deep cold water. The second component may be thought of as a net transport of heat by a warm western boundary current moving poleward compensated by a return flow of colder water on the eastern side of the ocean. This physical picture is oversimplified, but roughly correct for the flow fields of the model.

The meridional cell component is usually thought of as due to thermohaline circulation, but this does not take into account the important contribution of wind. Zonal wind stress can cause a net Ekman transport of surface water poleward in the trade wind zone, and equatorward in the zone of westerly winds. If we examine the meridional circulation in Fig. 11 we see that the meridional circulation in the tropics is largely associated with Ekman suction at the equator. The cells on either side of the equator are very effective in the poleward transport of heat, since the surface waters in the tropics are very warm relative to water at deeper levels. At low latitudes thermohaline forces and the wind work in the same direction to produce a meridional cell, but in the westerly zone thermohaline forces and wind oppose one another. This tends to weaken the meridional cell in the westerly zone and push it down to deeper levels. It also makes it less effective for transporting heat.

A horizontal circulation gyre will generally be less effective in transporting heat poleward than a circulation cell in the meridional vertical plane that has the same strength in terms of volume transport. This is because variations in temperature in the east-west direction along latitude circles are generally much less than the temperature difference between surface and deep water. The horizontal diffusion component of poleward heat transport simulates the effect of baroclinic instability in mixing heat down-gradient. There is good evidence that this process is important in the Gulf Stream, but little is known about it in less well explored parts of the ocean. At this point it is premature to emphasize any oceanographic interpretation of this mode of heat transport.

In Table 6 and in Fig. 12 the total heat transport of the model in the Northern Hemisphere is compared with two estimates based on observations. The first estimate by Sellers (1965) is based on the heat balance of the ocean surface, largely drawn from the computations of Budyko *et al.* (1962). The second estimate by Vonder Haar and Oort (1973) is based on the heat balance of the free atmosphere, using recent satellite data for the radiation contribution. The heat transport by the model appears to be too low, amounting to only 50% of the Sellers estimate and about 30% of that by Vonder Haar and Oort. One common feature to all three heat transport estimates is that the maximum transport is in lower latitudes. This feature is in marked contrast to the poleward transport of heat by the atmosphere, which has a maximum near 45° from the equator.

An explanation for this difference is given by the fractional contribution of various types of heat transport shown in Table 5 on the left. The gyre contribution has a relatively small contribution at all latitudes. The diffusion component is only dominant at high latitudes where the total heat transport itself is quite small. The dominant mechanism is the meridional cell component. If this is also true for the real ocean, a good explanation exists for the low-latitude maximum of heat transport.

TABLE 6. The total poleward heat transport (10^{19} cal day^{-1}) compared to estimates by Sellers (1965) and Vonder Haar and Oort (1973). On the left, the fractional contribution is given for three components of poleward transport. The sum of the fraction contributions is unity. Note the dominance of the meridional cell.

	Fractional contribution			Total poleward heat transport		
Latitude (N)	Meridional cell	Gyre component	Diffusion	Present model	Sellers (1965)	Vonder Haar and Oort (1973)
80	0.0	−0.5	1.5	0.0	0.0	−0.3
70	0.1	0.0	0.9	0.0	0.3	0.0
60	0.2	0.1	0.7	0.3	0.8	0.0
50	0.3	0.2	0.5	0.8	1.6	2.5
40	0.3	0.2	0.5	1.4	2.2	4.4
30	0.5	0.2	0.3	1.6	3.3	5.2
20	1.0	0.0	0.0	1.9	3.3	7.1
10	1.3	−0.2	−0.1	1.6	2.2	3.8
0	1.2	0.0	−0.2	0.5	−0.5	0.5

Only at low latitudes do the wind and thermohaline driving forces cooperate to produce a net flow of warm surface water poleward.

8. Concluding remarks

A joint ocean-atmosphere model has been allowed to seek a climatic equilibrium over the equivalent of 270 years in the ocean time scale. Initially the ocean is in a state of complete rest and the fields of temperature and salinity are uniform horizontally. The initial vertical distribution of temperature and salinity corresponds to an observed average for the world ocean. Solutions for the final 50 years of the numerical integration are compared with observations. The model predicts a reasonable surface temperature distribution, with respect to latitude, but fails to predict low enough temperatures in the polar regions. This is partly due to the lack of seasonal variations in the model which does not allow the extremes of winter cooling at higher latitudes which are actually observed.

A uniform value of vertical mixing for temperature and salinity is taken to be 0.3 cm^2 s^{-1}. The associated thermocline is quite a bit deeper than observed, but it is not clear whether this is due to the choice of mixing coefficient or the apparent weakness of the thermohaline circulation compared to estimates from observations. The independent prediction of the salinity field and its response to net evaporation minus precipitation at the surface is a very important element of the climatic model, since the true density field of the ocean is determined by temperature and salinity, not just by temperature alone. The model correctly predicts that the surface salinity of the Atlantic is higher than the Pacific, and it further predicts that the South Pacific is saltier at the surface than the North Pacific. A serious discrepancy in the salinity pattern is the protrusion of the Arctic halocline down into the Norwegian and Greenland Sea. This feature effectively blocks the penetration of the Gulf Stream into this area, forcing it to flow nearly due eastward across the North Atlantic. Interestingly enough, the circulation is much more like that published by Weyl (1968) for the last ice age than the present.

The major western boundary currents show up clearly in the ocean model, even though the surface wind-stress distribution is somewhat different than that observed, particularly in the Southern Hemisphere. Like other low-resolution models of the ocean circulation, the transports of the western boundary currents closely correspond to that given by the linear theory for a barotropic ocean. As a result, the calculated transports are considerably underpredicted. It is known that inertial effects and bottom torques associated with the baroclinic structure can enhance western boundary currents, and these effects can be included in higher resolution experiments. It should also be feasible to include the effects of Reynolds stresses due to Rossby waves once this effect is firmly confirmed by field measurements.

The simplified ice model fails to predict a proper export of ice from the Arctic Ocean which results in an excessive buildup in that area. Otherwise the area distribution of pack ice is quite realistic. Most of the pack ice is in the Northern Hemisphere. In the Southern Hemisphere only a small amount of pack ice is predicted, which is consistent with the rather small amount of perennial pack ice actually observed near Antarctica.

An analysis of the poleward heat transport by ocean currents in the model indicates that the most important mechanism is a net overturning in the vertical meridional plane. Warm surface waters moving poleward are compensated by a deeper colder current moving toward the equator. In the trade wind region the Ekman drift and the thermohaline circulation tend to reinforce each other to produce a strong flow of surface waters poleward. In middle latitudes the Ekman drift due to the westerlies opposes the thermohaline circulation so the poleward flow of surface water is much impeded. In the Northern Hemisphere the meridional cell in middle latitudes is pushed downward and becomes much less effective in transporting heat poleward. Thus the meridional cell mechanism for transporting heat poleward is most effective in tropical latitudes. It is concluded that this is the reason that the heat balance studies of Sellers (1965) and Vonder Haar and Oort (1973) show the maximum poleward heat transport by ocean currents at a latitude of only 20 to 30N, while the maximum transport by the atmosphere is at a much higher latitude.

Overall, the circulation may be described as "lazy." The interaction with the atmosphere is qualitatively correct, but the intensity is low compared to observations. For example, the poleward heat transport in the Northern Hemisphere is 30–50% of what is estimated by heat balance requirement based on atmospheric data.

New calculations are presently underway in which the flux of momentum, heat and water are specified from observations over the entire model world ocean. Although the calculations are not complete, the results show that with realistic boundary conditions, which include seasonal heating, the model gives a remarkably good simulation of the water mass structure of the ocean as it is actually observed. The intensity of the western boundary currents is less than observed, but nearly twice that of the present model. These preliminary results suggest that seasonal effects must be included in any future studies to test the full potential of a joint atmosphere-ocean climatic model.

APPENDIX A

Approximate Treatment of Velocity Time Scales

In the equations of an ocean circulation model there are a great many time scales, but we are mainly interested in the very long term adjustment of the ocean to wind stress and heating. For this reason it is reasonable to sacrifice accuracy in the higher frequency components in order to obtain the most efficient method for calculating the longer term adjustment of the ocean. There are two well-recognized approaches to this problem. One is to filter out high-frequency motions by altering the primary equations. For example, the rigid-lid approximation in the present model eliminates shallow-water, external gravity waves, travelling at a speed of $(gH)^{\frac{1}{2}}$. Another standard approach is the use of implicit finite-difference approximations. The 'implicit' schemes do not remove unwanted signals, but allow them to be treated in an approximated way so that even if they are not properly resolved by the time step of the numerical integration, instability will not occur. In other words, the Courant-Friedrichs-Lewy condition can be violated. If the high-frequency modes have a small amplitude and do not interact with the ocean circulation, the numerical integration can proceed with large time steps using an implicit method.

Table A1 provides some information on the most rapid signal for various components of the flow. Since external gravity waves have been filtered out of the model, the most rapid signal in the external model (vertically averaged velocity) are Rossby waves. The frequency of Rossby waves increases with increasing scale. The largest scale Rossby waves that can exist in the world ocean is a free mode for the entire Pacific basin. This mode has a 2-day period and an associated propagation speed of ~ 100 m s^{-1}. In the internal mode inertial motions are retained. Inertial motion has a minimum period of 12 h, but an implicit treatment of the Coriolis terms (Bryan, 1969) makes it unnecessary to resolve this particular type of oscillation in detail. Thus it is possible to use a time step considerably longer than the 0.15 day given in Table A1. The density field depends on temperature and salinity. These fields are sensitive to internal gravity waves, but due to the coarse horizontal resolution of the model these waves cannot be excited easily. Thus the main factor in changing the density field is horizontal and vertical advection by large-scale currents. Diffusion is also important, but the most stringent condition imposed on the time step is due to the horizontal velocity.

TABLE A1. Restrictions on the maximum allowable time step imposed by various components of the ocean circulation model. Δx is taken as 500 km.

	External mode	Internal mode	Temperature salinity
Symbol	$\bar{v}$	$\hat{v}$	θ, S
Most rapid signal	Rossby wave	Inertial wave	Advection
Speed (cm s^{-1})	10^4	—	10^2
Maximum stable time step ($\Delta t = C^{-1}\Delta x$)	0.05 day	0.15 day	5 day

TABLE A2. Values of coefficients of the local time derivatives of various components of the numerical circulation.

	Δt	2 days
External mode velocity	α	23.03
Internal mode velocity	β	8.64
Density	γ	1.00

We assume that only the local time derivatives of the finite-difference form of the equations of the model need be written out explicitly, i.e.,

$$\alpha\frac{(\bar{v}^{n+1}-\bar{v}^{n-1})}{2\Delta t}=G^n, \tag{A1}$$

$$\beta\frac{(\hat{v}^{n+1}-\hat{v}^{n-1})}{2\Delta t}=F^n, \tag{A2}$$

$$\gamma\left[\frac{(\theta^{n+1}-\theta^{n-1})}{2\Delta t}, \frac{(S^{n+1}-S^{n-1})}{2\Delta t}\right]=H^n, J^n, \tag{A3}$$

where $\bar{v}$ and $\hat{v}$ represent the vertically averaged mode and the baroclinic mode, respectively. For a detailed calculation of the time-dependence of the model, α, β and γ should all be equal to unity. In this case the time step must be adjusted to be compatible with the highest wave velocity in the system given in Table A1. In the present study we are only interested in the long-term adjustment of the density field, and not in the details of the adjustment of the velocity field to the density field. The values of Δt, α and β adopted are shown in Table A2. In the case that the model proceeds to a completely steady state this procedure is exact because all the local time derivatives vanish. It can be interpreted physically as a distortion of the model which slows down high-speed transient waves in the velocity field by a factor of 10 or more, without affecting geostrophic balance or stationary waves in a large-scale current. Numerical

tests of the accuracy have been carried out by Semtner (1973) with good results. The approximate method outlined here is a simple way to greatly increase the efficiency of large-scale models, but should not be used in cases where time scales less than one year are of importance.

APPENDIX B

The Relation between Reynolds Number and the Computational Mode

To illustrate the relation between Reynolds number and the computational mode, Chen (1971) considers the simplest possible case, the steady-state form of Burger's equation:

$$U\rho_x - A\rho_{xx} = 0. \tag{B1}$$

If the derivatives are expressed as centered differences,

$$(R-2)\rho_{j+1} + 4\rho_j - (R+2)\rho_{j-1} = 0, \tag{B2}$$

where $R = U\Delta/A$. The general solution may be written as

$$\rho_j = C_1 + C_2\xi^j. \tag{B3}$$

Substituting (B3) into (B2), we obtain

$$(R-2)\xi^2 + 4\xi - (R-2) = 0. \tag{B4}$$

The two roots of (B4) are

$$\xi = 1, \quad (2+R)/(2-R). \tag{B5}$$

A computation mode appears where ξ is negative, since ξ^j alternates in sign at adjacent grid points. The condition that ξ is positive definite is that $R<2$. This is equivalent to

$$\frac{U\Delta}{A} < 2. \tag{B6}$$

REFERENCES

Bryan, K., 1963: A numerical investigation of a nonlinear model of a wind-driven ocean. *J. Atmos. Sci.*, **20**, 594–606.

——, 1969: A numerical method for the study of the circulation of the world ocean. *J. Comput. Phys.*, 4, 347–376.

——, and M. D. Cox, 1968: A nonlinear model of an ocean driven by wind and differential heating. *J. Atmos. Sci.*, **25**. 945–978.

——, and ——, 1972: An approximate equation of state for numerical models of ocean circulation. *J. Phys. Oceanogr.* **2**, 510–514.

Budyko, M. I., N. A. Epinova, L. I. Zubenok and L. A. Strokina, 1962: The heat balance of the earth's surface. *Izv. Akad, Nauk. SSSR Geograf. Ser.*, No. 1, 6–16.

Chen, J-H., 1971: Ph.D. thesis, Princeton University, 102 pp.

Cox, M. D., 1970: A mathematical model of the Indian Ocean. *Deep Sea Res.*, **17**, 47–75.

Hamon, B. V., 1965: The East Australian Current, 1960–1964. *Deep Sea Res.*, **12**, 899–921.

Hellerman, S., 1967: An updated estimate of wind stress on the world ocean. *Mon. Wea. Rev.* **95**, 607–627 (see correction, 1968: **96**, 63–74).

Holland, W. D., and A. Hirschman, 1972: A numerical calculation of the circulation in the North Atlantic Ocean, *J. Phys. Oceanogr.*, **2**, 336–354.

Keondjian, V. P., 1972: Diagnostic calculation of current velocities on 16 levels in the North Atlantic. *Izv. Atmos. Oceanic Phys.*, **8**, 1297–1307.

Kraus, E. B., and J. S. Turner, 1967: A one-dimensional model of the seasonal thermocline: II. The general theory and its consequences. *Tellus*, **19**, 98–106.

Manabe, S., and K. Bryan, 1969: Climate calculations with a combined ocean-atmosphere model. *J. Atmos. Sci.*, **26**, 786–789.

——, —— and M. Spelman, 1975: A global ocean-atmosphere climate model. Part I. The atmospheric circulation. *J. Phys. Oceanogr.* **5**, 3–29.

Munk, W. H., 1950: On the wind-driven ocean circulation. *J. Meteor.*, **7**, 79–93.

——, 1966: Abyssal recipes. *Deep Sea Res.*, **13**, 707–730.

Osborne, T. R., and C. S. Cox, 1972: Ocean fine structure. *Geophys, Fluid. Dyn.*, **3**, 321–346.

Reid, J. L. Jr., 1965: *Intermediate Waters of the Pacific Ocean.* The Johns Hopkins Oceanographic Studies, No. 2, The Johns Hopkins Press, 85 pp.

——, and W. D. Nowlin, Jr., 1971: Transport of water through the Drake Passage. *Deep Sea Res.*, **18**, 51–64.

Rooth, C., and H. G. Östland, 1972: Penetration of tritium in the Atlantic thermocline. *Deep Sea Res.*, **19**, 481–492.

Sarkisyan, A. S., 1966: *Theory and Calculation of Ocean Currents.* Leningrad, Gidrometeoizdat. (English translation IPSR Press, Jerusalem, 1969; available from NTIS, Springfield, Va.)

Sellers, W. D., 1965: *Physical Climatology.* The University of Chicago Press, 272 pp.

Semtner, A. J., 1973: A numerical investigation of Arctic Ocean circulation. Ph.D. thesis, Princeton University, 251 pp.

Smith, S. M., H. W. Menard and G. Sharman, 1966: World-wide ocean depths and continental elevations averaged for area approximately one degree squares of latitude and longitude. Scripps Inst. Oceangr., Ref. 65–80, 14 pp.

Stommel, H., 1948: Westward intensification of wind-driven ocean currents. *Trans. Amer. Geophys. Union*, **29**, 202–206.

——, and J. Webster, 1962: Some properties of thermocline equations in a subtropical gyre. *J. Marine Res.*, **20**, 42–56.

Sverdrup, H. U., M. W. Johnson and R. H. Fleming, 1942: *The Oceans.* Prentice-Hall, 1060 pp.

Untersteiner, N., 1964: Calculations of temperature regime and heat budget of sea ice in the central Arctic. *J. Geophys. Res.*, **69**, 4755–4766.

Veronis, G., 1966: Wind-driven ocean circulation. *Deep Sea Res.*, **13**, 17–55.

Vonder Haar, T. H., and A. H. Oort, 1973: New estimate of annual poleward energy transport by Northern Hemisphere Oceans. *J. Phys. Oceangr.*, **2**, 169–172.

Warren, B. A., and G. H. Volkmann, 1968: A measurement of volume transport of the Gulf Stream south of New England. *J. Marine Res.*, **26**, 110–126.

Webster, T. F., 1961: The effect of meanders on the kinetic energy balance of the Gulf Stream. *Tellus*, **13**, 392–401.

Weyl, P., 1968: The role of the oceans in climatic change. *Meteor. Monogr.*, **8**, No. 30, 37–62.

Worthington, L. V., and H. Kawai, 1972: Comparison between deep sections across the Kuroshio and the Florida Current and Gulf Stream. *Kuroshio*, University of Washington Press, Chap. 10.